Supplement of Atmos. Chem. Phys., 21, 15199–15211, 2021
https://doi.org/10.5194/acp-21-15199-2021-supplement

Atmospheric Chemistry and Physics
Open Access

Supplement of

Dramatic changes in Harbin aerosol during 2018–2020: the roles of open burning policy and secondary aerosol formation

Yuan Cheng et al.

Correspondence to: Jiu-meng Liu (jiumengliu@hit.edu.cn)

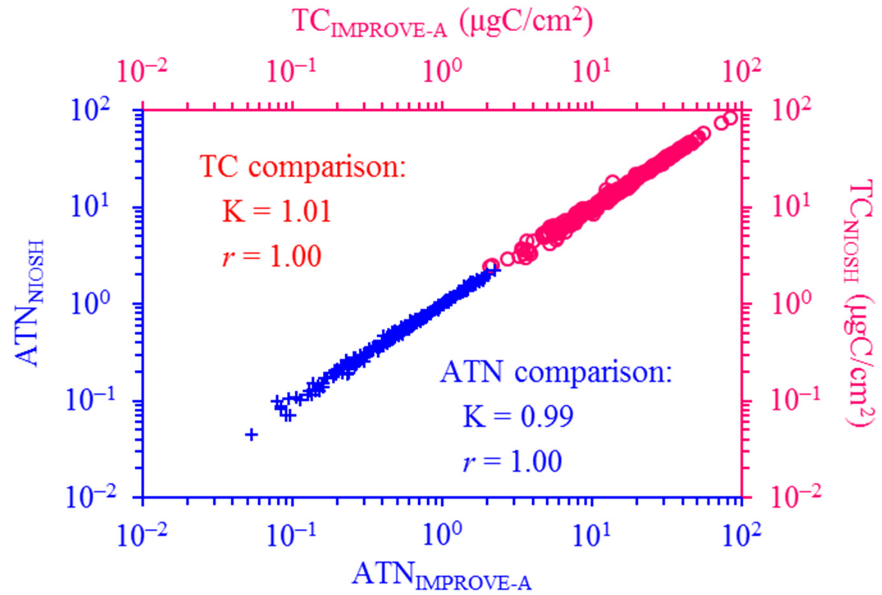

Figure S1. Comparisons of total carbon (TC) and optical attenuation (ATN) measured by different temperature protocols. Results from both campaigns are included. ATN is calculated as $\ln(I_{final}/I_{initial})$, where $I_{initial}$ and I_{final} indicate filter transmittance signals measured at the beginning (i.e., when the loaded filter has not been heated) and end (i.e., when all the deposited carbon has been combusted off the filter) of thermal-optical analysis, respectively. Linear regression results are shown with K as slope (intercept was set as zero). TC and ATN agreed well between different protocols, demonstrating good precisions for both the carbon and transmittance measurements.

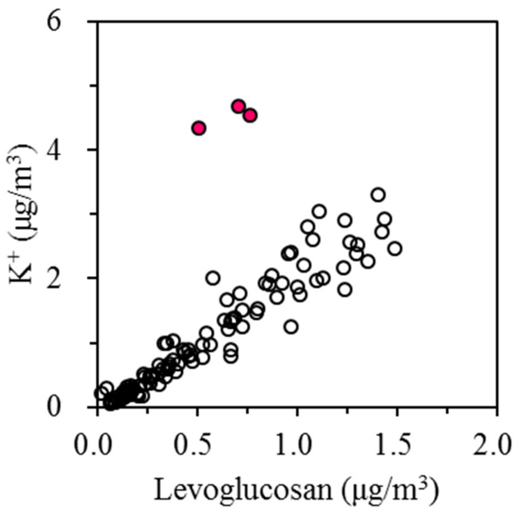

Figure S2. Relationship between K^+ and levoglucosan during the 2019–2020 campaign. Three samples collected during the Chinese New Year period exhibit substantially higher K^+ to levoglucosan ratios (as highlighted by the solid circles), pointing to significant influence of firework emissions.

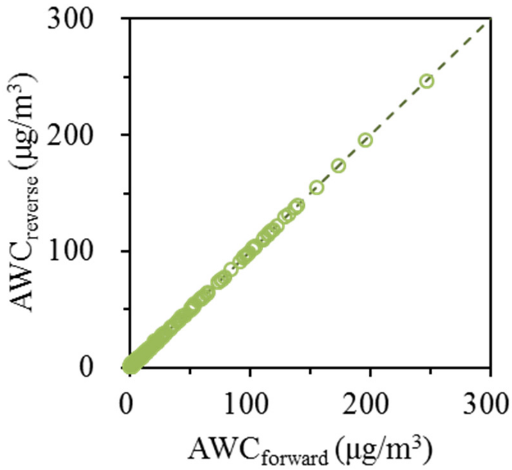

Figure S3. Comparison of AWC results predicted by reverse and forward modes. The dashed line indicates one-to-one correspondence.

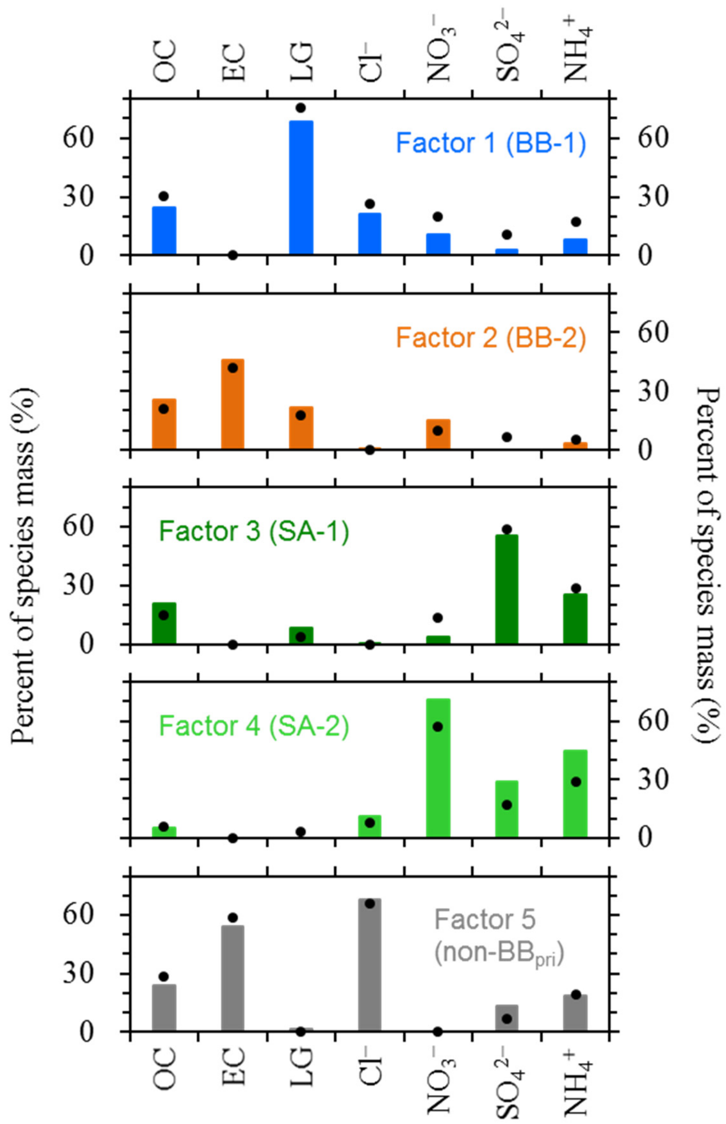

Figure S4. Source profiles resolved by PMF. The solid bars and circles indicate results obtained by this study and Cheng et al. (2021a), respectively. For this study, aerosol compositions measured during the 2018–2019 and 2019–2020 campaigns were combined and used as the PMF inputs, whereas Cheng et al. (2021a) was based only on the former campaign. In general, similar profiles were resolved by the two studies, despite the different measurement periods covered.

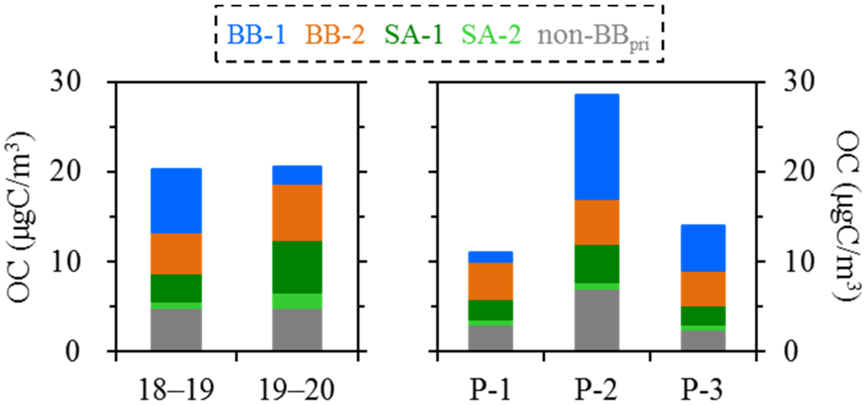

Figure S5. Comparisons of OC source apportionment results between the 2018–2019 and 2019–2020 campaigns (left panel), and across the 2018–2019 samples collected before (P-1), during (P-2) and after (P-3) the "legitimate burning" periods (right panel).

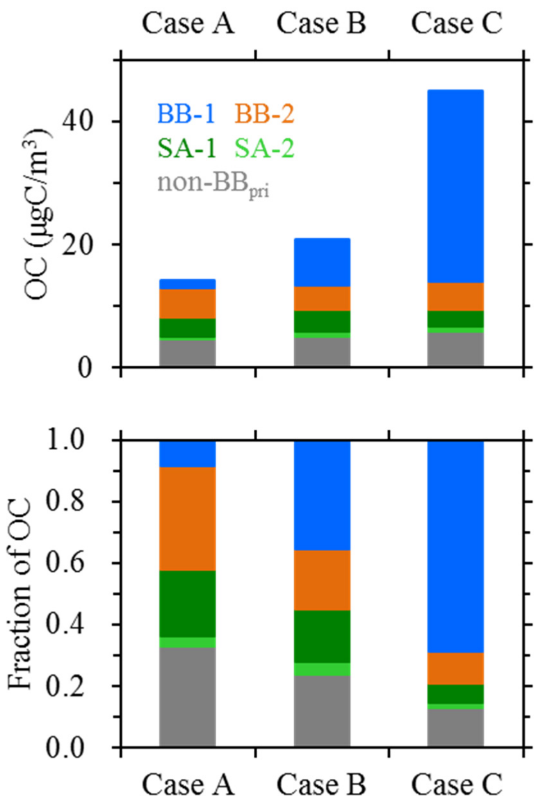

Figure S6. Comparison of OC source apportionment results across the 2018–2019 samples with increasing strengths of biomass burning impact. Cases A, B and C correspond to LG/OC ranges of < 1.5%, 1.5–3.0% and > 3.0%, respectively.

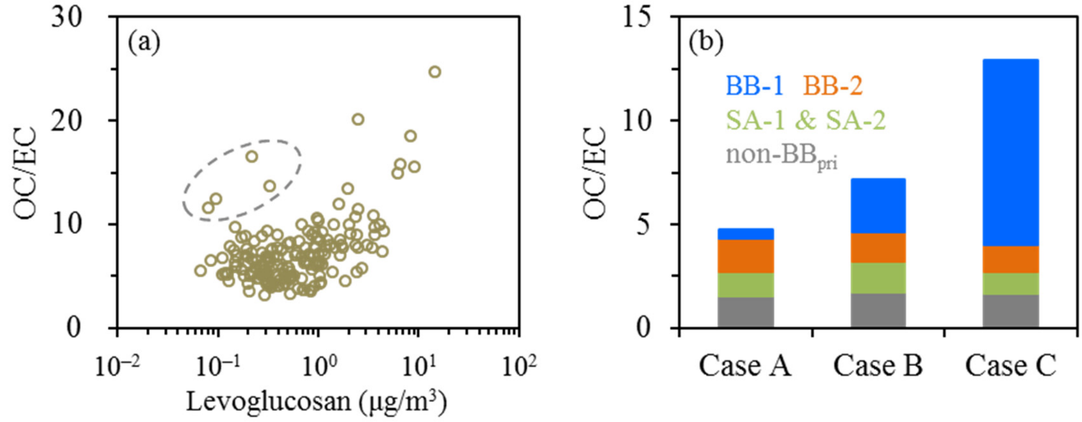

Figure S7. (a) Relationship between OC/EC and levoglucosan, and **(b)** comparison of OC/EC among Cases A–C, for the 2018–2019 campaign. OC/EC ratios in (b) are based on results from PMF analysis, i.e., for each case, OC/EC is presented as the sum of source-resolved OC to total EC ratios (e.g., OC_{BB-1}/EC and OC_{BB-2}/EC). The two factors representing secondary aerosols are not distinguished in (b). In general, OC/EC showed a positive dependence on levoglucosan, although there appeared to be several outliers (as highlighted by the dashed oval) which had the lowest EC concentrations of the measurement period (below ~0.5 μg/m^3). Thus, biomass burning is considered the dominant driver for the temporal variation of OC/EC during the 2018–2019 campaign. This inference is also supported by (b), as OC/EC exhibited an increasing trend from Case A through Case C, which cannot be explained by SOA or non-BB emissions.

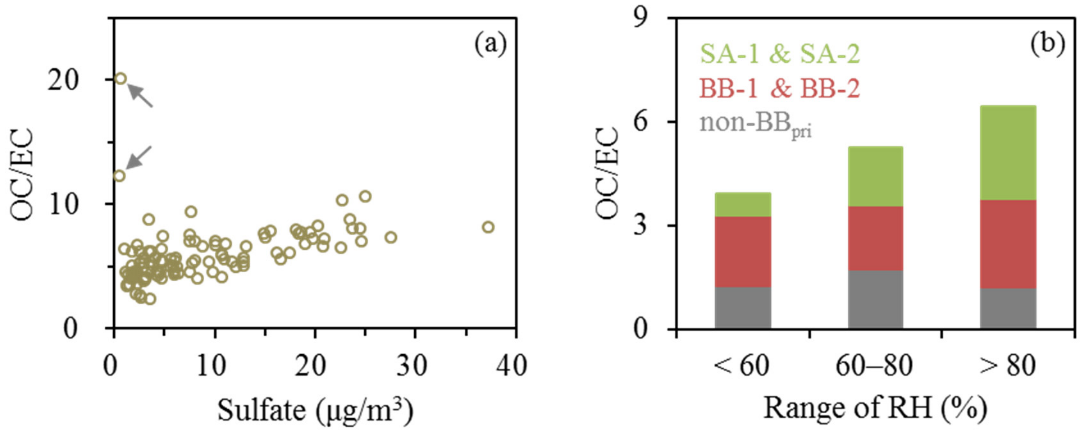

Figure S8. (a) Relationship between OC/EC and sulfate, and **(b)** comparison of OC/EC with increasing RH levels, for the 2019–2020 campaign. In general, OC/EC showed a positive dependence on sulfate, although there were two outliers (as highlighted by the arrows) which had the lowest EC concentrations of the measurement period (below 0.3 μg/m^3). Thus, SOA is considered the dominant driver for the temporal variation of OC/EC during the 2019–2020 campaign. This inference is also supported by (b), as with increasing RH, OC/EC exhibited an increasing trend, which cannot be explained by the primary factors (either BB or non-BB).

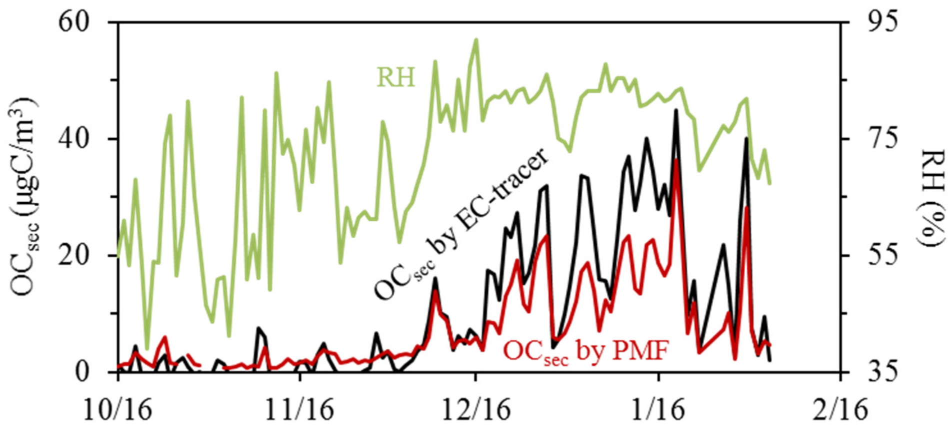

Figure S9. Temporal variations of OC_{sec} and RH during the 2019–2020 campaign. The PMF-based OC_{sec} was calculated as the sum of OC masses attributed to the SA-1 and SA-2 factors. For the EC-tracer method, OC_{sec} was calculated as: $OC_{sec} = OC - EC \times (OC/EC)_{pri} - OC^*$, where $(OC/EC)_{pri}$ is the OC to EC ratio representative of combustion sources and OC^* indicates primary OC from non-combustion sources. For the 2019–2020 campaign, $(OC/EC)_{pri}$ and OC^* were determined based on linear regression of OC on EC ($r = 0.98$), with $(OC/EC)_{pri}$ as the slope (2.13) and OC^* as the intercept (3.11), respectively, using low-RH samples (i.e., those with RH below 60%). Compared to the PMF-based results, OC_{sec} calculated by the EC-tracer method showed a similar pattern of temporal variation. Results from both methods showed RH-dependent increase of OC_{sec}.

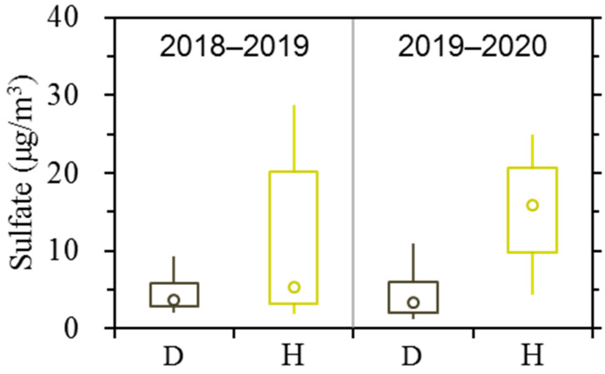

Figure S10. Comparison of sulfate between different RH levels for the 2018–2019 and 2019–2020 campaigns. The terms “D” and “H” indicate relatively dry and more humid conditions with RH below and above 80%, respectively.

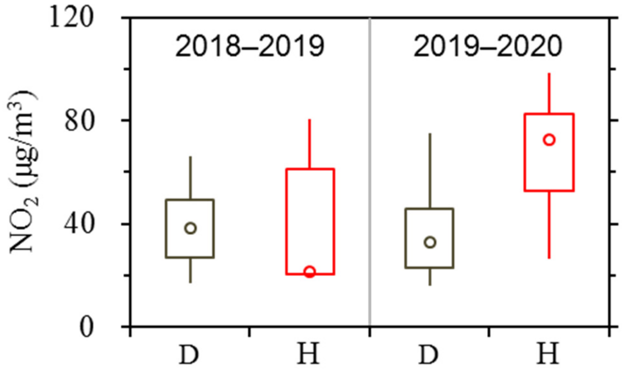

Figure S11. Comparison of NO_2 between different RH levels for the 2018–2019 and 2019–2020 campaigns.

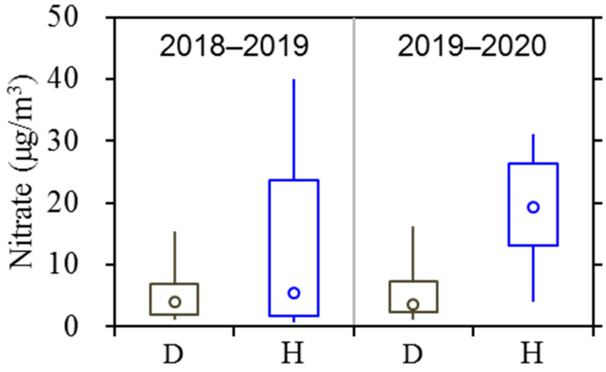

Figure S12. Comparison of nitrate between different RH levels for the 2018–2019 and 2019–2020 campaigns.

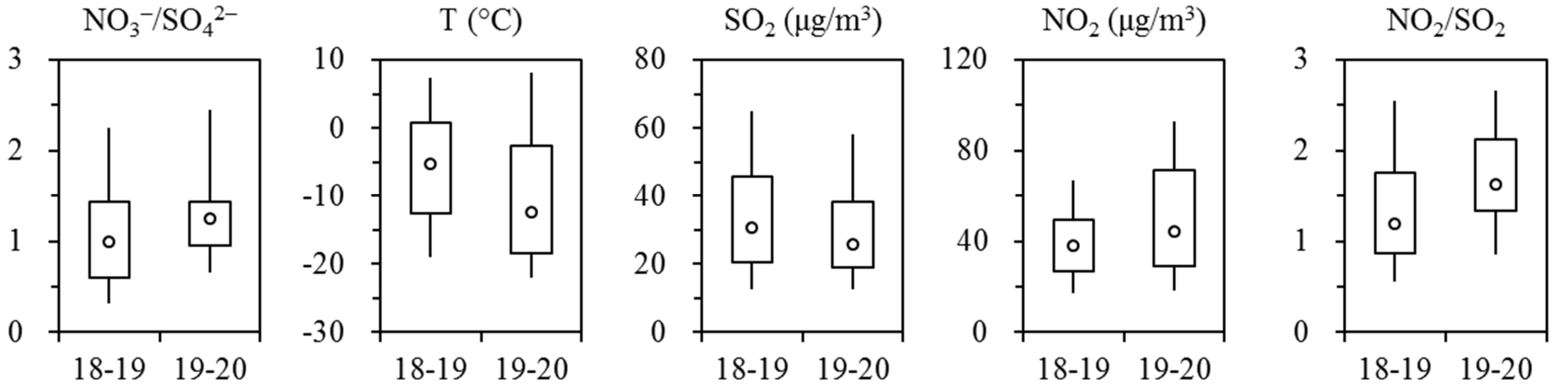

Figure S13. Comparisons of the nitrate to sulfate ratios, temperatures, SO_2, NO_2 and the NO_2 to SO_2 ratios between the 2018–2019 and 2019–2020 campaigns.

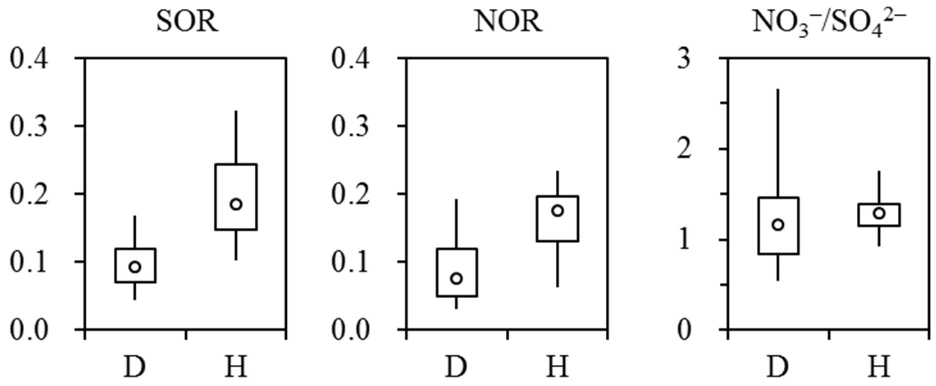

Figure S14. Comparisons of SOR, NOR and the nitrate to sulfate ratios at different RH levels for the 2019–2020 campaign.

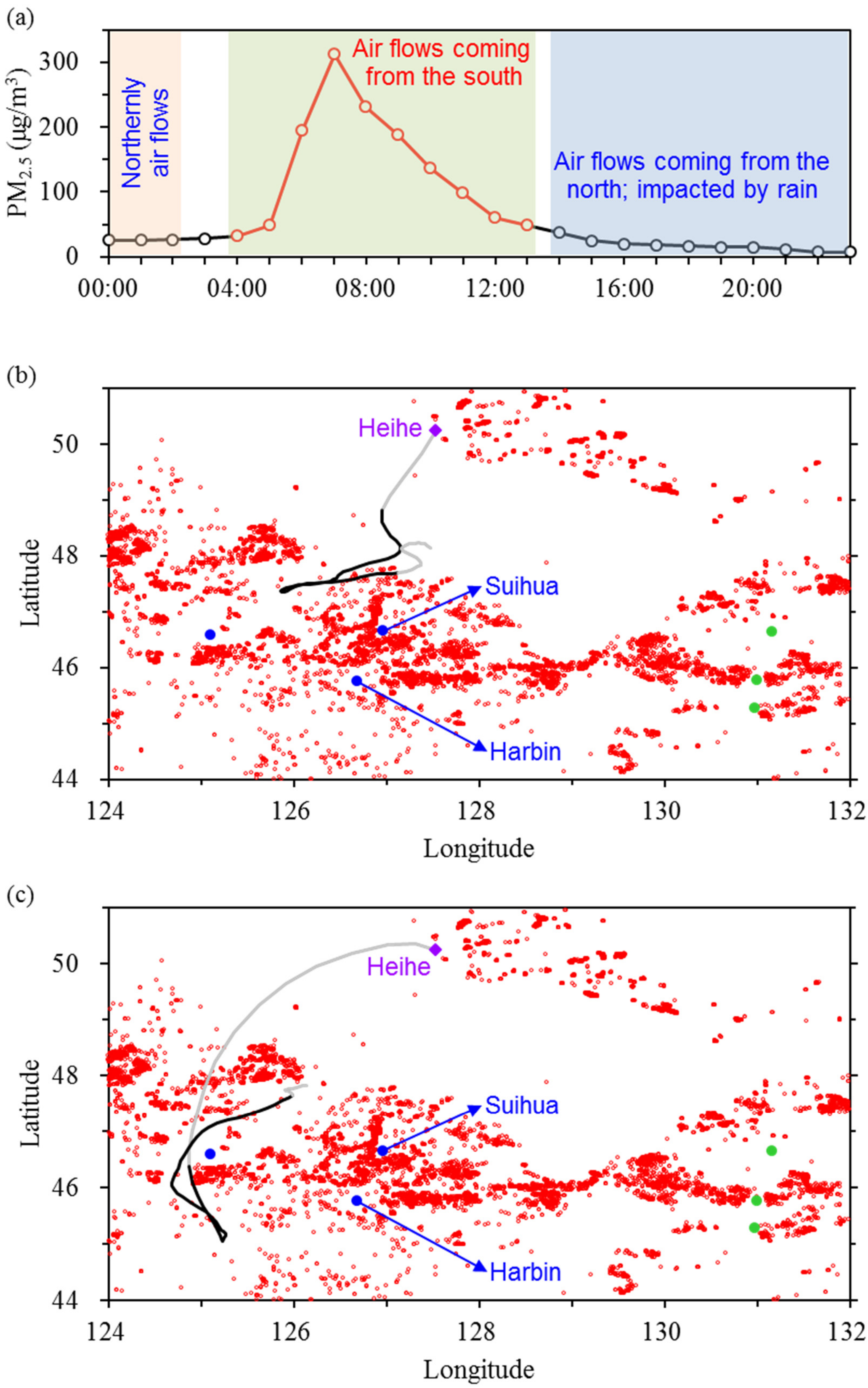

Figure S15. (a) Temporal variation of 1-h $PM_{2.5}$ observed in Heihe on 19 April, 2020. **(b–c)** 72-hour back trajectories ending at 4:00 and 13:00, respectively, in Heihe, overlaid with active fires detected during 17–18 April, 2020 as red circles. $PM_{2.5}$ were relatively low between 0:00 and 3:00, when the air flows came from the northwest, moved fast and descended sharply. $PM_{2.5}$ started to increase at 4:00, with the trajectory from the south and impacted by the region with agricultural fires (as shown in b). The increase of $PM_{2.5}$ continued as the trajectory path moved towards Harbin and Suihua, where the impacts of open burning were inferred to be extremely strong based on their off-the-chart $PM_{2.5}$ concentrations. The maximum $PM_{2.5}$ was observed at 7:00, and then $PM_{2.5}$ started to decrease although the air masses still passed over the Harbin-Suihua region (or the nearby area) before arriving at Heihe. A likely cause for the decrease of $PM_{2.5}$ after 7:00 was the increase of planetary boundary layer height from morning through noon time. The trajectory left the Harbin-Suihua region at 13:00 (as shown in c) and returned to the north at 14:00. In addition, there was rain in Heihe after 14:00, and correspondingly, $PM_{2.5}$ gradually decreased to below 10 $\mu g/m^3$.